




Fabrication of lightweight and biodegradable EMI shield films with selective distribution of 1D carbonaceous nanofiller into the co-continuous binary polymer matrix

Krishnendu Nath¹, Suman Kumar Ghosh¹, Palash Das¹, Ankur Katheria¹, and Narayan Ch. Das^{1,*} 

¹ Rubber Technology Centre, Indian Institute of Technology, Kharagpur 721302, India

Received: 24 October 2022

Accepted: 2 March 2023

Published online:
17 March 2023

© The Author(s), under exclusive licence to Springer Science+Business Media, LLC, part of Springer Nature 2023

ABSTRACT

The solvent mixing process is a utile production technique to promote the cost-effective preparation of lightweight and flexible electromagnetic interference (EMI) shield films based on binary polymer-based conductive nanocomposite material with a very low electrical percolation threshold. Here in, a facile preparation of conductive binary biodegradable polymer nanocomposite films comprised of ester-based thermoplastic polyurethane (TPU), and poly (butylene adipate -co-terephthalate) (PBAT) is reported where the acid-functionalized multiwalled carbon nanotube (MO) has been preferentially incorporated into the PBAT phase of the binary polymer matrix and to get effective nanofiller dispersion we employed solvent mixing technique. For the effective reduction of “e-wastes” biodegradability is new generation demand for polymer nanocomposites. The PBAT/TPU based biodegradable binary blend has not been used before to fabricate polymer nanocomposite material. The 0.8 mm thick polymer nanocomposite film with the loading of around 5 wt% of MO is considered as the nanocomposite film achieving the electrical percolation threshold indicated by a sudden jump in the total EMI shielding effectiveness (EMI SE) value from – 17 to – 24 dB (within the frequency region from 8.2 to 12.4 GHz) if the MO content is upgraded from 3 to 5 wt%. A loading of 10 wt% of MO gives – 30 dB of EMI SE at 8.2 GHz. The preferential distribution of MO filler in the PBAT phase has been confirmed by FTIR, DMA, selective dissolution test, HRTEM, and FESEM characterization techniques.

Address correspondence to E-mail: ncdas@rtc.iitkgp.ac.in

1 Introduction

The scientific demonstration of the effectiveness of lightweight polymer nanocomposite materials as EMI shields is in the twenty-first century with innovative applications based on the art of inclusion of conductive nanofillers into the flexible polymer matrix. Before going further deep into the matter we need to first discuss some of the harmful effects which are imparted by the electromagnetic wave. EM waves evolving from adjacent electronic devices interact with each other and create noises causing damage to their performances [1]. EM wave also causes harmful health hazards [2] (e.g., cancer, headaches, neurological disorders, etc.). After analyzing all the negative effects imposed by electromagnetic waves on mankind; nanotechnologists are constantly proposing as well as modifying the solution that inhibits the propagation of EM waves through the encasing of electronic devices by making the latter electrically conductive. The metallic encasing being electrically conductive, could be a good option to be used as an EM wave absorber but the problem is the weight of the encasing which is too high to be used in lightweight electronic items (e.g., laptops, mobiles, etc.). Now the question is how to make a polymer matrix conductive. The answer is nanofillers which are electrically conductive and could be included in the polymer matrix to turn it into a conductive one. There are different types of nanofillers such as natural fibres [3], single-walled carbon nanotubes (SWCNTs) [4], multi-walled carbon nanotubes (MWCNTs) [5], graphene oxides (GO) [6], reduced graphene oxides (RGO) [7], carbon nanofibers (CNF) [8], etc. Since its inception [9, 10], carbon nanotubes have shown their potential to be used as an electrically conductive agent in the electrically insulating polymer matrix to make polymer nanocomposites [11, 12]. The potential use of carbon nanotube-based polymer nanocomposites as an EM wave shield material [13–15] gradually came into the light. Chauhan et al. [16] incorporated MWCNTs into the poly (ether-ketone) (PEK) matrix applying the melt mixing process and only 17 wt% of MWCNT had given EMI shielding efficiency around – 38 dB in Ka-band (26.5–40 GHz). Mei et al. [17] incorporated CNT films into an epoxy matrix to get excellent EMI shielding effectiveness (52 dB). Jeevananda et al. [18] had synthesized polyaniline in presence of MWCNT particles to get poly-

aniline/ MWCNT nanocomposites which showed good electrical conductivity. Monnereau et al. [19] demonstrated foamed polycarbonate (PC)/MWCNT nanocomposites in presence of supercritical carbon dioxide to achieve better EMI shielding performance than PC/MWCNT nanocomposites that were not foamed. Jang et al. [20] had polymerized cyclic butylene terephthalate (CBT) in presence of MWCNT to get enhanced EMI shielding efficiency of around 30 dB. The modern-day research on EMI shield material revolves around the accomplishment of the co-continuity of polymer phases of binary polymer blends in which the conductive carbon nanotubes are preferentially distributed in a particular polymer phase or at the interface depending upon the surface energy difference [21] between nanofiller and melt viscosity difference between polymers of the blends [22–24] to achieve very low electrical percolation threshold to promote cost effectivity in the production of conductive polymer nanocomposites. Nunes et al. developed linear low-density polyethylene (LLDPE)/poly (ethylene-co-methyl acrylate (PEMA))/CNT-based composites to modify the electrical percolation threshold to a lower value where the hybrid polymer matrix gave higher electrical conductivity compared to the neat polymer nanocomposite [25]. Kunjappan et al. [26] proposed polymer nanocomposite based on poly-(trimethylene terephthalate) (PTT) along with polyethylene (PE) and MWCNT to get the latter dispersed into the PTT phase where only 3 wt% of MWCNT gave EMI shielding efficiency around 32 dB. Dou et al. had shown that MWCNT particles are preferentially distributed into the low viscous (melt) polystyrene phase situated in the interface between the co-continuous high-density polyethylene (HDPE) phase and polyvinylidene fluoride (PVDF) phase of HDPE/PVDF based binary co-continuous blend and only 1.2 wt% of the nanofiller had given EMI shielding effectiveness of 31 dB [27]. Nowadays, the focus of nanotechnology is shifting to green chemistry and “e-waste” [28] or electronic waste, and to reduce the latter, the polymer matrix could be made out of a biodegradable one. In our previous work [1], we had reported poly (lactic acid) (PLA)/ thermoplastic polyurethane (TPU) based biodegradable binary polymer blend as the polymer matrix and conductive carbon black (VCB) was used to make the polymer matrix conductive and the polymer nanocomposites had shown good EMI effectiveness. Dispersibility of

the conductive filler into the polymer matrix is an essential matter to improve mechanical as well as electrical properties. The chemical functionalization of MWCNT increases its dispersibility (into the polymer matrix) which improves both the chemical and mechanical properties of the polymer matrix [12]. Among different types of chemical functionalization, oxidation or purification of MWCNT is very common and was found to increase electrical conductivity [29] of the oxidized MWCNT-based polymer nanocomposite. The solvent mixing/casting technique to process polymers improves the overall dispersibility of the nanofiller into the polymer matrix [30] more effectively. The combination of TPU and PBAT as a biodegradable binary polymer blend was never been presented extensively before. In the present work, we have chosen TPU and PBAT to produce biodegradable polymer blends (based on the melt viscosity difference at processing temperature) exploiting the solvent mixing and casting technique using tetrahydrofuran (THF) as the solvent for both the polymer. Though PBAT is brittle, combining TPU with the former boosts the mechanical properties of the blend/nanocomposite. The blend with a 50:50 weight ratio of PBAT/TPU was found to be co-continuous into which laboratory modified (oxidized) MWCNT (MO) was incorporated employing solvent mixing technique to produce polymer nanocomposites with a loading of 10 wt% of MO with a thickness of 0.8 mm giving -30 dB of shielding efficiency at 8.2 GHz of frequency. The enzyme-mediated biodegradability as well as mechanical properties, electrical properties, and EMI shielding properties of polymer nanocomposites have been studied and reported rationally in this work.

2 Experimental

2.1 Materials

PBAT (density = 1.22 g/cc; purity 98.9%) was supplied by Huainian Ruanketrade Co. China. Ester-based TPU (density = 1.2 g/cc; purity 99.8%) was supplied by Covestro India under the trade name Desmopan 385E ®. Conductive carbon black (VCB) was supplied by Cabot Corp India under the trade name Vulcan XC-72 (surface area = 180 m²/g). Pristine MWCNT (surface area = 330 m²/g and bulk density of 0.25–0.35 g/cc) was supplied by United

Nanotech Innovations Pvt Ltd. Anhydrous (purity 99.9%) THF was supplied by Sigma Aldrich Chemicals Pvt. Ltd. Pseudomonas lipase enzyme was procured from Sigma Aldrich (Lipase from *Pseudomonas cepacia*).

2.2 Modification (oxidation) of pristine MWCNT

Generally, pristine MWCNT is modified/ oxidized to increase the dispersibility of de-coiled MWCNT in the polymer nanocomposite [31]. The process [32] which has been followed to oxidize MWCNT is the treatment of pristine MWCNT with concentrated HNO₃ and H₂SO₄. In a typical process, 30 mg of pristine MWCNT was treated with an ultrasonicated (frequency of 40 kHz, ultrasonic power of 120 W) in 10 ml of a mixture of concentrated HNO₃ and H₂SO₄ (in a weight ratio of 3:1) for 7 h. in a water bath inside of an ultrasonicator kept at 60 °C.

2.3 Preparation of TPU/PBAT blends for rheological analysis

Blends of TPU and PBAT of different compositions are prepared using solvent mixing and casting technology to check the viscosity of the pure polymers and polymer blends at processing/compression molding temperature (170 °C). In a typical process, required masses of polymers are dissolved in a pre-determined volume of THF under a magnetic stirrer (at 60 °C). After, the polymer solutions were mixed and kept for 1 h. under the magnetic stirrer at the temperature of 60 °C. Then, the polymer mixtures were cast on petri-dish and kept overnight for air drying before the compression molding at 170 °C to polymer blend sheets (thickness = 0.8 mm). The polymer blends are designated as T_XP_Y (X = mass fraction of TPU and Y = mass fraction of PBAT). The polymer blend compositions are given in Table 1.

2.4 Preparation of TPU/PBAT/MO nanocomposites

The solvent mixing and casting technology are employed to prepare polymer nanocomposites [33]. In a typical process, the required quantity of both TPU and PBAT polymers are dissolved in THF solvent upon a magnetic stirrer under a temperature of 60 °C according to the polymer compositions given in

Table 1 Composition of TPU and PBAT in the polymer blends (T_XP_Y)

Polymer nanocomposite designation	Mass of TPU in the nanocomposite sheet(g) (in 20 ml THF)	Mass of PBAT in the nanocomposite sheet (g) (in 20 ml THF)	Mass of MO in the nanocomposite sheet (g) (in 20 ml THF)
$T_{100}P_0$	4.0	0	0
$T_{80}P_{20}$	3.2	0.8	0
$T_{70}P_{30}$	2.8	1.2	0
$T_{60}P_{40}$	2.4	1.6	0
$T_{50}P_{50}$	2.0	2.0	0
$T_{40}P_{60}$	1.6	2.4	0
$T_{30}P_{70}$	1.2	2.8	0
$T_{20}P_{80}$	0.8	3.2	0
T_0P_{100}	0	4.0	0

T thermoplastic polyurethane, P poly (butylene adipate -co-terephthalate)

The polymer blends have been represented as T_XP_Y where X = Wt% of T and Y = Wt% of P .

Table 1. Parallely, the required quantity of MO was also suspended in THF by employing an ultrasonication process for 1.5 h. Then both the polymer solution PBAT in THF and TPU in THF were blended and mixed under magnetic stirring for 1 h. Then, the MO/THF suspension is mixed with a polymer solution and kept under stirring for 1 h. to prepare the polymer nanocomposite solution. After, the polymer nanocomposite solution was cast on a petri dish and kept for air drying to get unmolded polymer nanocomposite sheet which was later compression molded under 5000 psi of pressure and 170 °C temperature to get the polymer nanocomposite sheets (thickness = 0.8 mm) and designated as $T_XP_YMO_Z$

where X , Y , and Z stands for wt% of each of TPU, PBAT and MO respectively (Table 2). The fabrication procedure of the polymer nanocomposite is depicted in Fig. 1.

2.5 Materials characterization

The capillary rheometer 'smart RHEO 2000' with a bore diameter of 15 mm and barrel length of 290 mm was used to detect melt viscosities of TPU/PBAT blends at the processing temperature of 170 °C. X-ray diffraction (XRD) analysis of pristine MWCNT and MO particles was carried out using 'X'PERT PRO (PAN analytical B. V, The Netherlands)' machine using Ni-filtered Cu K_α radiation ($\lambda = 0.154$ nm) in

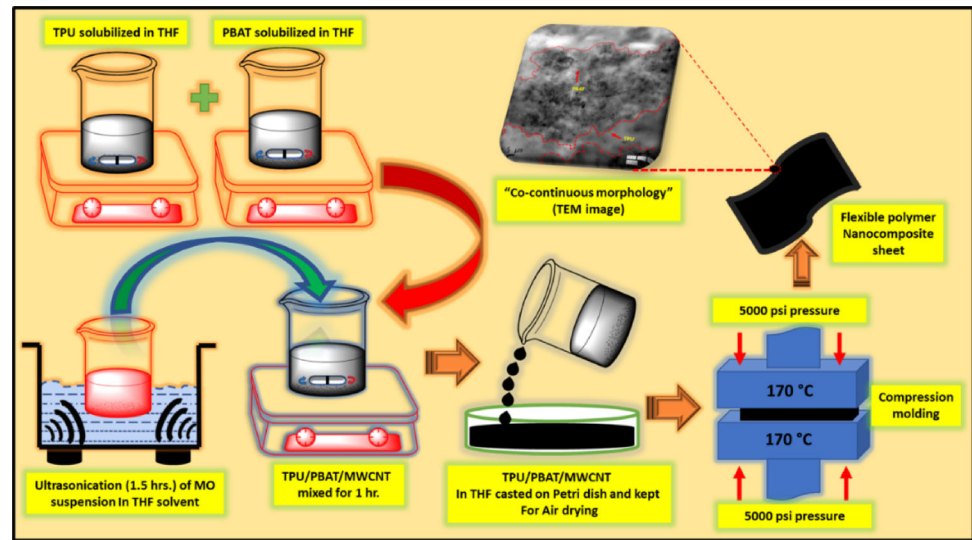
Table 2 Composition of TPU, PBAT, and MO in the polymer nanocomposites ($T_XP_YMO_Z$)

Polymer nanocomposite designation	Mass of TPU in the nanocomposite sheet (g) (in 20 ml THF)	Mass of PBAT in the nanocomposite sheet (g) (in 20 ml THF)	Mass of MO in the nanocomposite sheet (g) (in 20 ml THF)
$T_{100}P_0MO_0$	2.0	0	0
$T_0P_{100}MO_0$	0	2.0	0
$T_{50}P_{50}MO_0$	1.0	1.0	0
$T_{50}P_{50}MO_2$	1.0	1.0	0.04 ± 0.001
$T_{50}P_{50}MO_3$	1.0	1.0	0.06 ± 0.001
$T_{50}P_{50}MO_5$	1.0	1.0	0.1 ± 0.01
$T_{50}P_{50}MO_7$	1.0	1.0	0.14 ± 0.001
$T_{50}P_{50}MO_{10}$	1.0	1.0	0.2 ± 0.01

T thermoplastic polyurethane, P poly (butylene adipate -co-terephthalate), MO oxidized MWCNT

The polymer blends have been represented as $T_XP_YMO_Z$ where X = Wt% of T , Y = Wt% of P , and Z = Wt% of MO

Fig. 1 Graphical representation of fabrication of polymer nanocomposites ($T_xP_yMO_z$) following solvent mixing and casting method



the 2θ range of 10° to 60° and the crystallite size of both pristine MWCNT and MO particles were determined using Debye–Scherrer equation [34] (Eq. 1).

$$D = \frac{K\lambda}{\beta \cos \theta} \quad (1)$$

Here D is the average crystallite size (in nm); K is dimensionless shape factor or Scherrer constant the value of which depends upon the crystallite shape and the size distribution, indices of the diffraction line, and the actual definition used for β whether FWHM or integral breadth [35]. K can have values anywhere from 0.62 and 2.08 and value of K is considered here is 0.95; θ is the Bragg angle where β is the width of the x-ray peak on the 2θ axis usually characterized as full width at half maximum (FWHM) after considering the error measurement due to instrumental broadening; λ is the x-ray wavelength. Fluctuations in the spatial orientation of walls of MWCNTs can also affect the width. In this work, we have calculated only the estimated values of D . (Discussion on the accuracy of Eq. (1) can be found in the literature, for example, in [36]). Raman spectroscopy analysis of pristine MWCNT and MO particles was carried out in Trivista 555 spectrograph (Princeton instruments). Field emission scanning electron microscopy (FESEM) of cryofabricated surfaces of the polymer nanocomposites and 50:50 TPU/PBAT blend were carried out on FESEM, Merlin, Carl ZEISS Pvt Ltd. The morphology of the TPU/PBAT blend (50:50) was also examined under FESEM by solubilizing/etching out the PBAT phase using

chloroform as a solvent for PBAT. The selective dissolution test was accomplished by dissolving 1.5 g of a polymer nanocomposite in chloroform (to etch-out PBAT phase) and in DMF (to etch-out TPU phase) and kept for 7–8 days to detect any change in the color of (blackening) of the solutions. MWCNT distribution in the polymer nanocomposite was further confirmed using a high-resolution transmission electron microscope (HRTEM) JOEL, JEM-2100F (operational voltage -200 kV). Before HRTEM analysis, ultra-cryomicroscopy was employed to cut the samples with thicknesses between 100 and 190 nm on a Leica Ultra Cut E M FCS under a nitrogen environment. Dynamic mechanical analysis (DMA) of the polymer nanocomposites was carried out in 'METRAVIB DMA 50 N' analyzer where the samples were cut in square form (length-10 mm, width-3 mm) of which the two ends were attached and the frequency of 5 Hz was applied and ran within the temperature range of -60°C to room temperature. The PerkinElmer SpectrumTM3 FT-IR spectrometer was employed to conduct FTIR spectroscopy within the range of 400 cm^{-1} to 4000 cm^{-1} with 32 scans. Hounsfield Universal Tensile testing machine (Hounsfield H10 KS) was exploited to measure tensile strength where dumbbell-shaped test pieces were cropped from a 1 mm thick polymer nanocomposite sheet and the tensile test was performed following ASTM D412-98 standard extended Mooney-Rivlin model was employed to study internal friction behavior of the polymer blends and nanocomposites. Thermal properties of polymer nanocomposites were carried out using a thermogravimetric analyzer

(TGA, Q5000, TA instrument, USA). Enzymatic degradation tests of the PBAT/TPU blend, as well as polymer nanocomposites, were accomplished using the enzyme *Pseudomonas lipase*. In a typical process cylindrical portions (diameter = 13 mm, thickness = 0.8 mm) were cut from the samples of blends and nanocomposites and kept in a vial containing 10 ml of 0.05 M buffer solution (pH = 7.0) and 0.9 mg of the enzyme under 37 °C of temperature for a predetermined time (10 days). For each kind of blend or composite three cylindrical samples were cut. The buffer test solution was changed every day. The average result is depicted in Fig. S4 (supporting information file). DC conductivity of the composites was measured by first determining the resistivity (σ_{res}) offered by the test samples using Eq. 1 given below. where A and h are the area and thickness respectively. R is the surface resistivity of the test samples. We could then find the conductivity in S/cm after taking the reciprocal of R .

$$\sigma_{res} = \frac{AR}{h} \quad (2)$$

The DC conductivity measurement was conducted on Keithley 6514 system electrometer. AC impedance of the composites was measured before the measurement of conductivity using a high-quality AC impedance analyzer 'Win Deta Novotherm α '. The range of frequency used for all of the readings was kept between 0 and 10 MHz keeping the potential difference of 1 V. The EMI shielding effectiveness (EMI SE) of the samples was calculated on the E5071C VNA series Vector network analyzer, Agilent Technologies, Inc., the USA in the X-band frequency range (8.2 GHz–12.4 GHz) the (error percentage < 3%). Nicholson-Ross-Weir (NRW) method was employed to calculate complex permittivity and permeability from S-parameters. In the experimental data plot the error bars (if any) are mentioned in terms of standard deviation w.r.t the data.

3 Results and discussion

3.1 Rheological properties of TPU/PBAT blends

The basis of this work depends upon the difference in melt viscosity of pure PBAT, TPU, and the polymer blends at the processing /compression molding

temperature of 170 °C as the surface energies of PBAT (43.24 mN/m) [37] and TPU (46 mN/m) [1], as a result, the filler will prefer the polymer phase with lowest melt viscosity at processing temperature to get distributed preferentially into it [38]. The study of melt viscosity is shown in Fig. 2.

Melt viscosity also decides the morphology of the polymer blends [39]. The maximum shear rate experienced by the polymer melt inside of a compression mold is around 10 s^{-1} [40]. The melt shear viscosity of pure TPU was found to be 258 MPa.s (Mega pascal second) whereas the same for PBAT was 114 MPa.s which is much less than that of the former one at 170 °C and 10 s^{-1} of shear rate. The melt viscosity of the polymer blends also decreases if portions of PBAT are increased at the particular shear rate of 10 s^{-1} . The melt shear viscosity was found to be decreasing with an increase in the shear rate for each of the pure polymers and polymer blends as usual. Due to the huge difference in polymer melt shear viscosity the polymers, PBAT and TPU are found to be immiscible blends and MO particles are preferentially distributed into the PBAT phase further confirmed by FESEM, HRTEM analysis, and selective dissolution test.

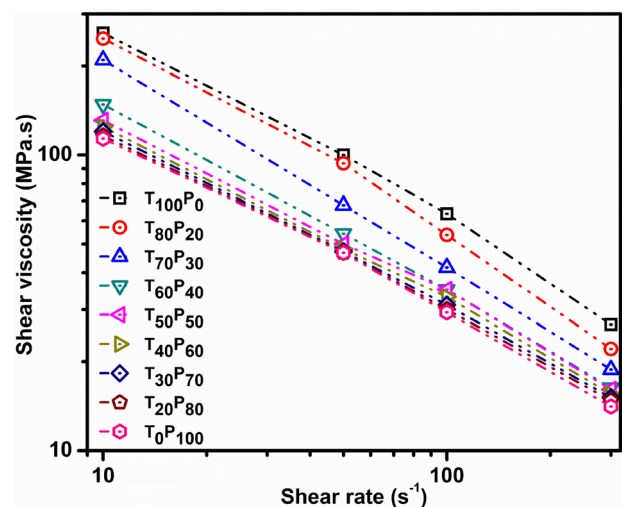


Fig. 2 Rheological study of TPU/PBAT blends at the processing temperature

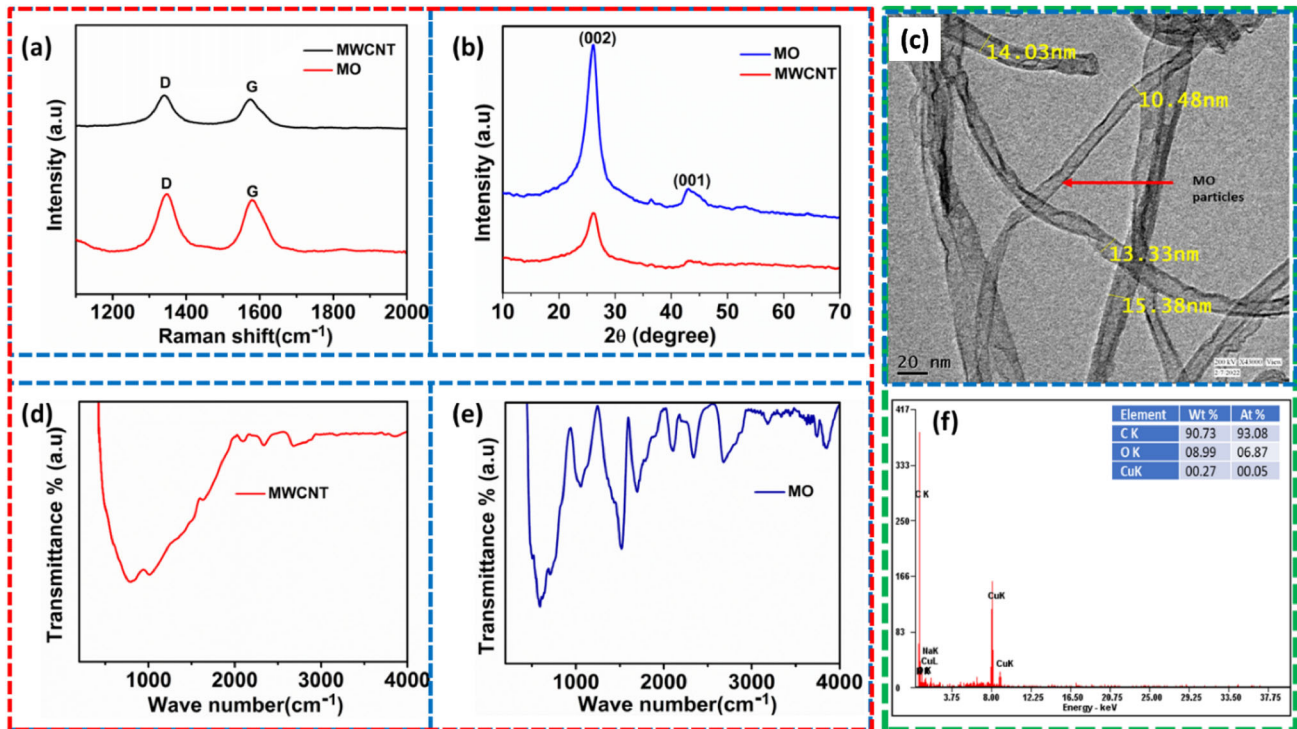


Fig. 3 **a** Raman spectroscopy of pristine MWCNT and MO, **b** XRD analysis of MO and pristine MWCNT, **c** HRTEM image of MO particles, **d** FTIR spectra of MO particles, **e** FTIR spectra of MWCNT particles, **f** EDAX analysis of MO particles

3.2 Structural analysis of MO particles using FTIR, Raman spectroscopy, XRD, and HRTEM characterization techniques

Figure 3 gives the FTIR analysis of pristine MWCNT and MO particles in Fig. 3e and d gives the identification of different types of chemical functional groups on the MWCNT surface before and after oxidation respectively. Figure 3d shows a sharp peak around 1700 cm^{-1} indicating the carbonyl stretching frequency of the carboxylic group justifying the formation of the latter on the MO particle surface [41]. Whereas, pristine MWCNT particle doesn't show any sharp peak regarding carboxylic group around 1700 cm^{-1} (Fig. 3e) instead a broad peak from 500 to 1990 cm^{-1} reveals a complex interaction between C–H stretching frequency, C=C stretching frequency, C–O–C stretching frequency, C–H out of the plane deformational frequency, C–O–H stretching frequency on the pristine MWCNT surface [42].

Figure 3a portrays the Raman spectroscopic analysis of pristine MWCNT and MO particles where the D-band at 1341 cm^{-1} and G-band at 1576 cm^{-1} give characteristic Raman peaks for crystalline graphitic

morphology [43] for both the particles. The intensity of D and G peaks in the case of MO particles is more compared to that of pristine MWCNT. The I_D/I_G ratio of MO and pristine MWCNT particles are 1.12 and 1.09 respectively revealing an increased number of defective sites due to acid functionalization on the MWCNT surface to get MO particles with an increased number of acid-functionalized groups. The findings from Raman spectroscopy have been further supported by XRD analysis (Fig. 3b) where two diffraction peaks around $2\theta = 26^\circ$ and 43° corresponding to (002) plane (001) of graphitic planes of MO is more intense than that of pristine MWCNT proving slightly higher inter-planar spacing is present on MO particles due to acid functionalization [44, 45]. Employing Debye–Scherrer equation (Eq. 1) [45] on (002) plane the crystallite size of both the pristine MWCNT and MO have been studied in the Table 3.

It is clear from the Table 3 that crystallite size of MO particles decreased slightly on chemical modification of pristine MWCNT. Figure 3c gives the HRTEM micrograph of MO particles with cylindrical structures of diameter in the range of 10–16 nm. The EDAX analysis of MO particles (Fig. 3f) shows almost

Table 3 Crystallite size determination using Scherrer equation

Sr No	Sample(s)	2θ	FWHM (β) (Radians)	$\cos\theta$	λ (nm)	D (nm) (for estimated $K=1$)
1	Pristine MWCNT	25	0.041	0.976	0.154	3.8
2	MO	26	0.044	0.974	0.154	3.6

9 wt % oxygen content claiming an ample amount of oxidation is being done on the surface of MWCNT particles.

3.3 Morphological analysis.

3.3.1 FESEM analysis of polymer blend/nanocomposites

The FESEM technique is an important electronic microscopic analytical tool to observe the phase morphology of polymer nanocomposites. Figure 4a portrays the FESEM micrographs of cryo-fractured and chloroform etched surface of the bulk of the polymer blend ($T_{50}P_{50}$) and the micrographic image reveals the co-continuity in the bulk of the polymer blend based upon which rest of the polymer nanocomposites were devised.

From Fig. 4b–e, it is observable that the MO particles of the polymer nanocomposites with 3, 5, 7, and, 10 wt% of MO content respectively are preferentially

distributed in the bulk of a particular polymer phase which is believed to be PBAT and the claim is supported by the viscosity study and the FTIR analysis. The selective distribution test where the chloroform solution turns black supports the claim that MO particles are preferentially distributed into the low viscous PBAT phase (Fig. 4f).

3.3.2 HRTEM analysis of polymer nanocomposites

The claims made by the FESEM study are further supported by HRTEM analysis as shown in Fig. 6 where the morphology of the bulk of the polymer nanocomposites is portrayed as cloud-like black portions which are believed to be the PBAT phase on which the larger portion of the MO particles are accumulated and the comparatively bright portions are believed to be TPU. From Fig. 5a–d it is obvious that a polar interaction between the chemical

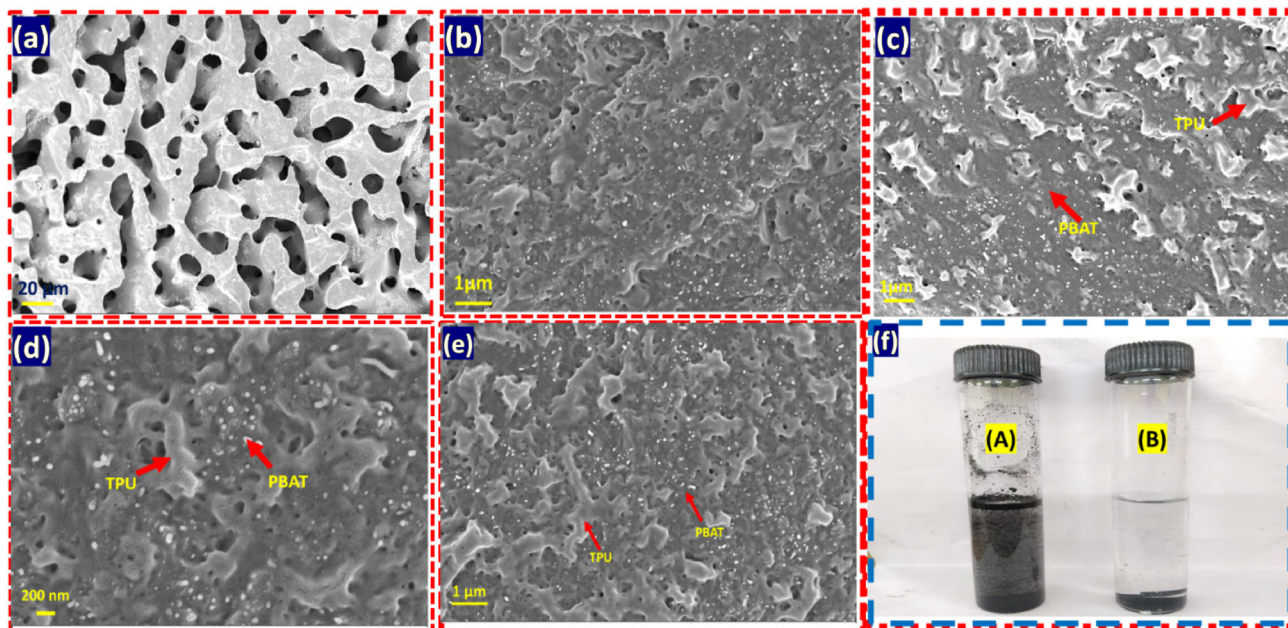
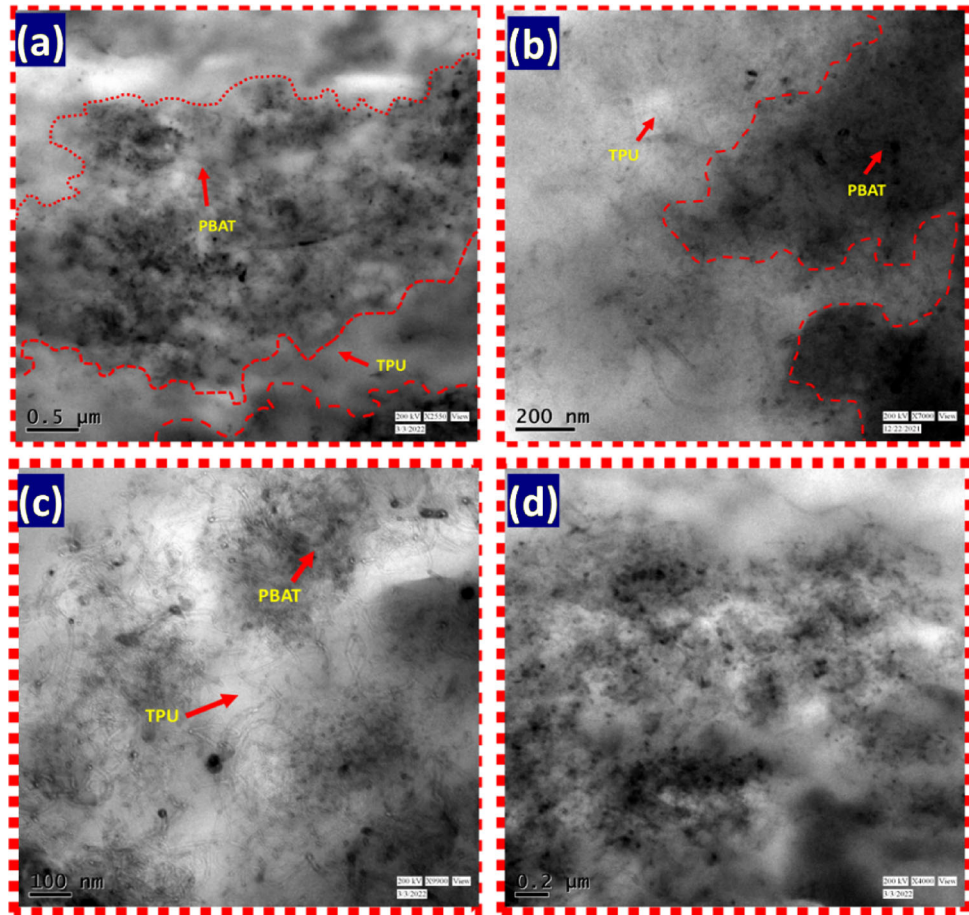


Fig. 4 a Cryo-fractured and etched surface of the bulk of the blend $T_{50}P_{50}$, b–e FESEM image of the cryo-fractured surface of the bulk of the polymer nanocomposites $T_{50}P_{50}MO_3$, $T_{50}P_{50}MO_5$,

$T_{50}P_{50}MO_7$ and, $T_{50}P_{50}MO_{10}$, f selective dissolution test of the polymer nanocomposite $T_{50}P_{50}MO_5$

Fig. 5 HRTEM micrograph of polymer nanocomposites
 a $T_{50}P_{50}MO_3$, and
 b $T_{50}P_{50}MO_5$, c $T_{50}P_{50}MO_7$,
 d $T_{50}P_{50}MO_{10}$



functional groups of MO particle surface and PBAT polymer chain throughout the bulk of the polymer matrix is proved to be present through electron microscopic analysis. Skimmed and localized conductive network all over the bulk of the polymer matrix results in a low electrical percolation threshold [21].

3.4 FTIR analysis of polymer nanocomposites

The FTIR analysis of the polymer nanocomposites and nanofiller particles gives information regarding the presence of different types of chemical functional groups in the polymer chain and the nanofiller surface and the interaction between them.

Figure 6a represents the FTIR spectrum of polymer blend and nanocomposites. The preferential distribution of MO particles in the PBAT phase could be justified by the disappearance of the FTIR peak related to carbonyl [46] ($C=O$) at 1710 cm^{-1} which was present in the blend $T_{50}P_{50}$ but disappeared in

polymer nanocomposites (Fig. 6b and f) due to plausible interaction of $-OH$ group of carboxylic groups with the carbonyl group of PBAT chain through hydrogen bonding [21] (Fig. 6e). Another way to claim the fact that MO particles are preferentially distributed in the PBAT and not in the TPU phase is by portraying the fact that the peak at 1535 cm^{-1} corresponding to N-H bending vibration frequency [47] is not disappeared and is still present at even 10 wt% of MO particles (Fig. 6c) in the polymer blend matrix. The major peaks of FTIR analysis of TPU [47] are as follows (Fig. 6d): sharp peak at 3327 cm^{-1} for N-H stretching frequency, peak at 1722 cm^{-1} for stretching vibration of carbonyl ($C=O$) group, sharp peak at 1535 cm^{-1} due to N-H bending vibration, peak at 2970 cm^{-1} for stretching frequency of aliphatic and aromatic C-H bond, 1457 cm^{-1} for C-H deformation, 651 cm^{-1} for N-H wagging, 1079 cm^{-1} for stretching vibration for C-O bond in the urethane group, etc. The major peaks of FTIR analysis of PBAT [48] are as follows (Fig. 6d): $C=O$ stretching frequency at 1710 cm^{-1} , a sharp peak

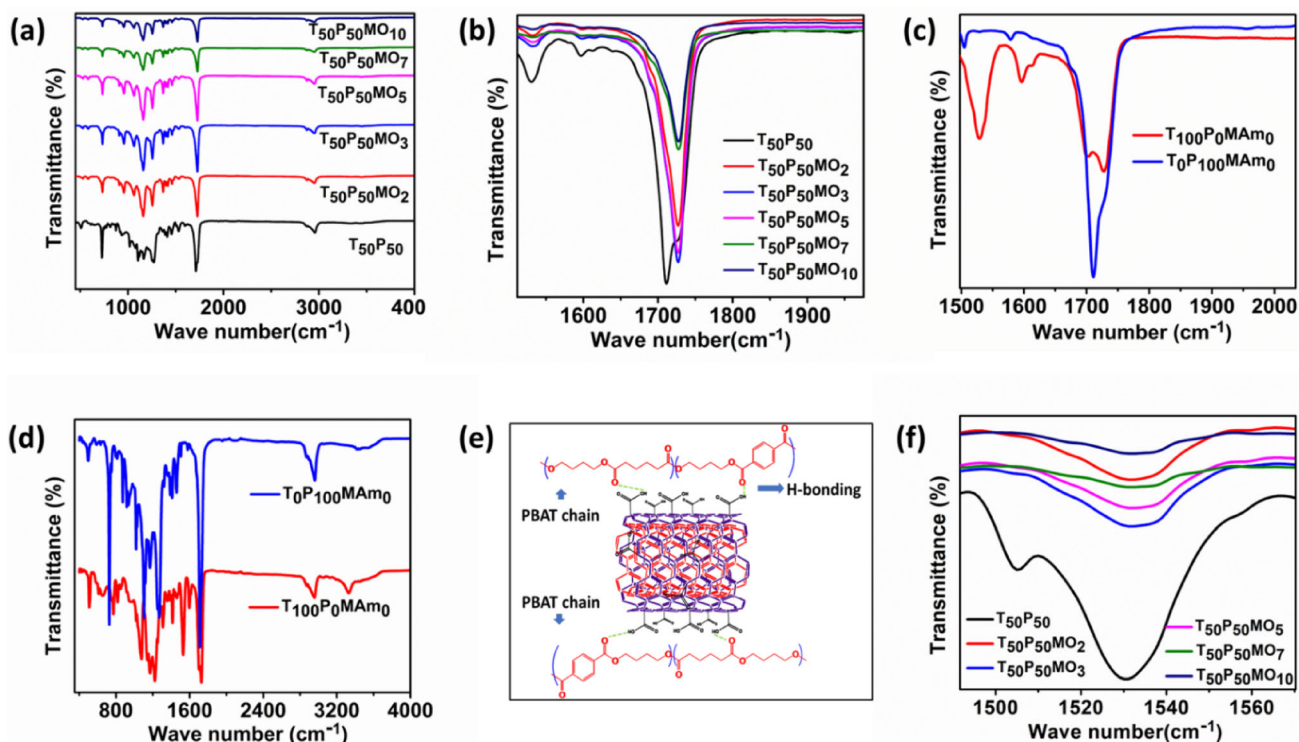


Fig. 6 **a** FTIR spectrum of TPU/PBAT (50:50) blend and TPU/PBAT/MO polymer nanocomposite, **b** Magnified FTIR spectrum of TPU/PBAT (50:50) blend and TPU/PBAT/MO polymer nanocomposite within the range 1470 cm^{-1} and 2000 cm^{-1} , **c** Magnified FTIR spectrum of TPU/PBAT (50:50) blend and TPU/PBAT/MO polymer nanocomposite within the range 1450 cm^{-1}

and 1620 cm^{-1} , **d** FTIR spectrum of the surface of pure TPU ($T_{100}P_0MO_0$) and pure PBAT ($T_0P_{100}MO_0$), **e** plausible interaction between carbonyl groups of both PBAT chain and MO surface through hydrogen bonding, **f** magnified FTIR spectrum of the surface of pure TPU ($T_{100}P_0MO_0$) and pure PBAT ($T_0P_{100}MO_0$) within the range 1500 cm^{-1} and 2060 cm^{-1} .

at 720 cm^{-1} methylene group ($-\text{CH}_2-$) vibration, a peak at 2970 cm^{-1} for stretching frequency of aliphatic and aromatic C–H bond, etc. The FTIR peaks of the blend $T_{50}P_{50}$ contain peaks from both the pure TPU and PBAT suggesting no chemical reaction between them. The selective distribution of MO particles within the PBAT of the binary polymer blend has been further supported by dynamic mechanical analysis (DMA) in Fig. S1 (supporting information file).

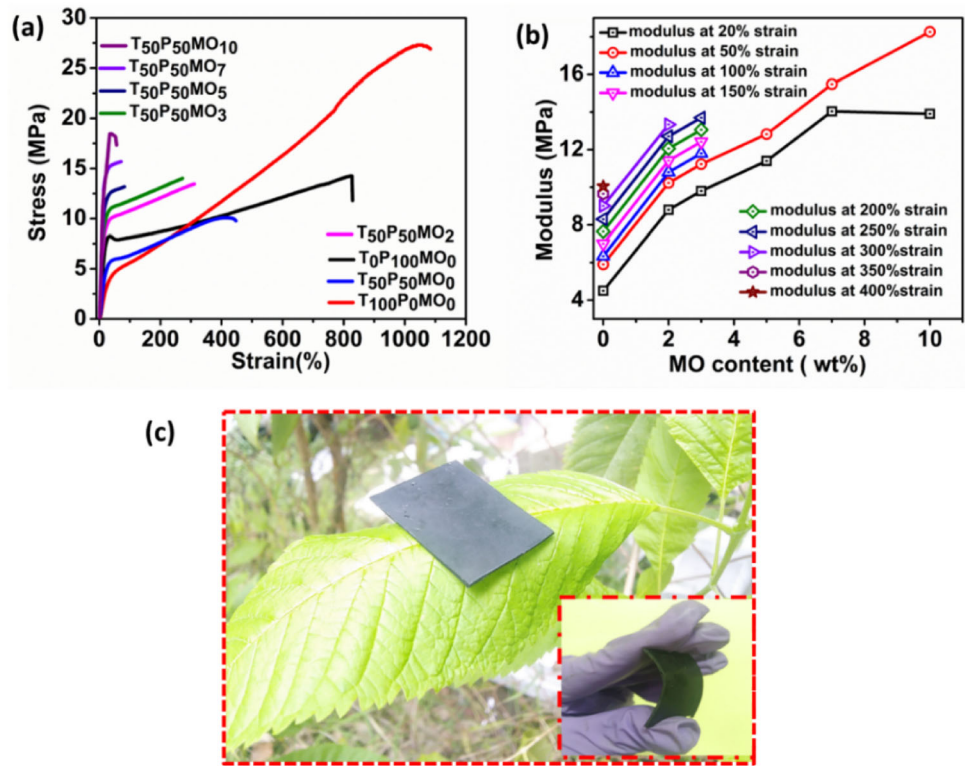
3.5 Mechanical properties

Nanofiller distribution in the bulk of the polymer matrix determines the mechanical/tensile strength of polymer nanocomposites. The tensile strength of a polymer nanocomposite is developed based mainly upon the following interactions: polymer -nanofiller, nanofiller-nanofiller. The mechanical strength of the polymer nanocomposites also depends upon the type of polymers used to formulate the nanocomposite.

Figure 7a describes the stress-strain behavior of the polymer nanocomposites ($T_xP_yMO_z$).

The pure TPU has better mechanical properties compared to the pure PBAT. TPU has the highest elongation at break (1084%) with the highest ultimate tensile strength of 27 MPa whereas PBAT has the elongation at break around 830% with the ultimate tensile strength of 12 ± 0.02 MPa. The $T_{50}P_{50}$ blend showed intermediate elongation at break (450%) and ultimate tensile strength (10 ± 0.01) MPa when compared to that of pure PBAT and TPU. With the gradual addition of MO, the ultimate tensile strength of the polymer nanocomposites improves and elongation at break decreases indicating nanofiller-nanofiller interaction increases significantly along with polymer-nanofiller interaction with the increment in the nanofiller quantity into the polymer blend matrix. The polymer nanocomposite with 10 wt% of MO loading ($T_{50}P_{50}MO_{10}$) showed the highest tensile strength around 19 MPa with the lowest elongation at break ($\sim 56\%$) indicating nanofiller -nanofiller

Fig. 7 a Stress–strain plots of TPU, PBAT, and their 50:50 blend and other polymer nanocomposites, b Change in tensile modulus (MPa) at a different elongation of polymer nanocomposites ($T_xP_yMO_z$) with the increment in filler loading, c photographic image of lightweight and flexible polymer nanocomposite (inset)



interaction is prevalent compared to the polymer-nanofiller interaction due to high nanofiller loading. Figure 7b portrays modulus at different percentages of strain for the polymer nanocomposites. It also describes the fact that the tensile modulus of the nanocomposites improves with MO loading compromising the elongation at break which decreases due to increased nanofiller-nanofiller interaction with the increment in MO loading. We have performed internal friction variation of the polymer blends and polymer nanocomposites using extended Mooney-Rivlin model [49]. The result of the study is shown in the supporting information file in detail (Section S5; Fig S5).

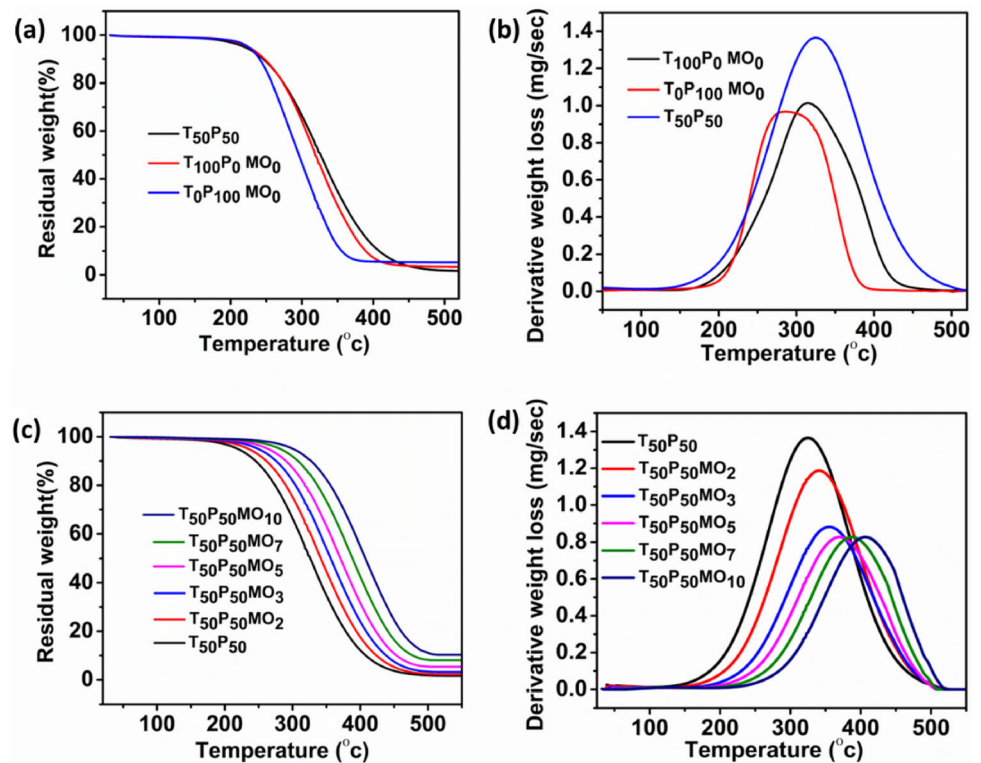
3.6 Thermogravimetric analysis (TGA)

The thermal stability of polymer nanocomposites at the decomposition temperature could be appropriately represented by thermogravimetric analysis which portrays the resistance to the thermal decomposition posed by the nanofiller present in the bulk of the polymer(blend) matrix due to polymer chain -nanofiller interactions. The thermogravimetric analysis could also give information about the composition of polymer nanocomposites. The

thermogravimetric analysis of polymer nanocomposites is shown below in Fig. 8.

Complete degradation of TPU, PBAT, and the blend $T_{50}P_{50}$ was found to be around 453 °C, 430 °C, and 445 °C (Fig. 8a). With the increase in MO content the polymer chain-nanofiller interactions increase which leads to more barriers to thermal degradation that is why polymer nanocomposites with higher MO content showed higher thermal degradation temperature (Fig. 8c). DTG plots shown in Fig. 8b and d give a better understanding of the degradation process where TPU and PBAT showed the maximum degradation temperature around 315 °C, 285 °C, and 322 °C. With the increase in MO content the maximum degradation temperature shifts to a higher value. The polymer nanocomposite with 10 wt% of MO content showed the highest value of maximum degradation temperature around 407 °C. The residue char of the thermally degraded polymer nanocomposite also increases with an increase in MO content. The heat resistance index is also an important parameter to observe the thermal degradation behavior of the polymer nanocomposites. The mathematical expression of heat resistance index could be presented as Eq. 2 given below [21] -

Fig. 8 **a** TGA thermograph, and, **b** DTG graph of pure polymers (TPU and PBAT) and TPU/PBAT (50:50) blend **c** TGA thermograph, and **d** DTG graph of TPU/PBAT (50:50) blend (for comparison) and polymer nanocomposites ($T_xP_yMO_z$)



$$HRI = 0.49[T_5 + 0.6(T_{30} - T_5)] \quad (3)$$

Here T_5 and T_{30} are the temperatures corresponds to 5% and 30% weight loss respectively due to thermal decomposition of the initial mass of the polymer nanocomposites. Table 4 represents the maximum degradation temperature and HRI values of single polymers, blends, and nanocomposites.

The polymer nanocomposites with 10 wt% of MO have shown the highest HRI value with the highest maximum degradation temperature due to the highest filler content.

Table 4 Thermal analysis data of polymer nanocomposites ($T_xP_yMO_z$)

Sample designation	T_5 (°C)	T_{30} (°C)	HRI	Maximum degradation temperature
$T_{100}P_0$	241	298	146	315
T_0P_{100}	250	284	139	285
$T_{50}P_{50}$	219	294	144	325
$T_{50}P_{50}MO_2$	235	310	152	341
$T_{50}P_{50}MO_3$	250	323	158	355
$T_{50}P_{50}MO_5$	264	339	166	370
$T_{50}P_{50}MO_7$	282	357	175	388
$T_{50}P_{50}MO_{10}$	301	376	184	407

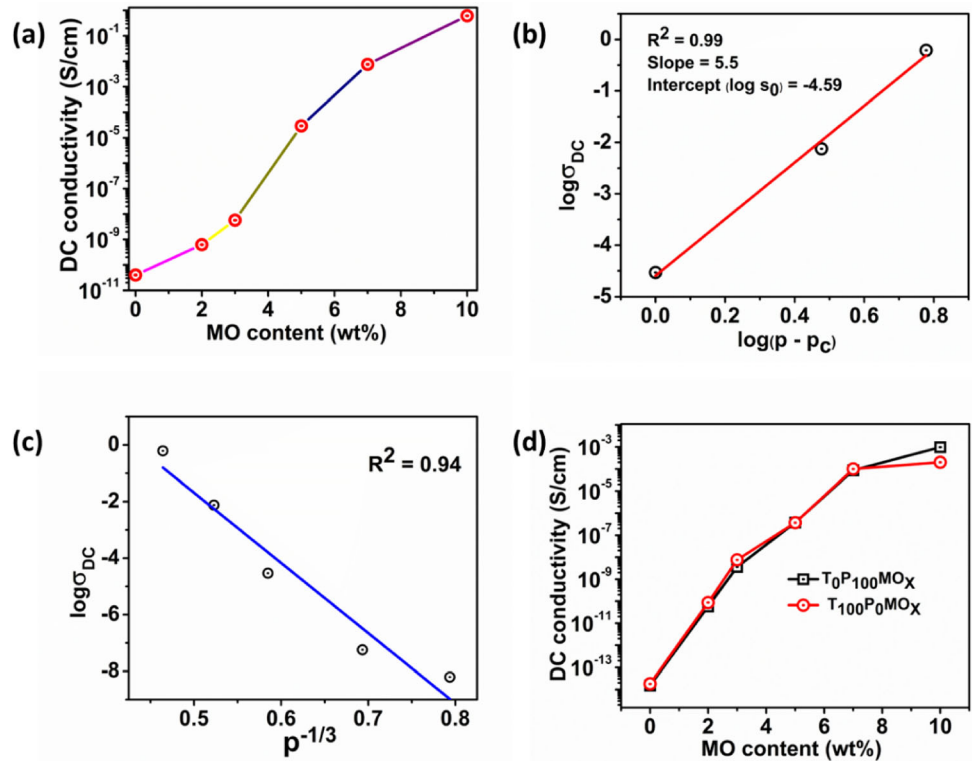
T thermoplastic polyurethane, P poly (butylene adipate -co-terephthalate), MO oxidized MWCNT
The polymer blends have been represented as $T_xP_yMO_z$ where X = Wt% of T, Y = Wt% of P, and Z = Wt% of MO

3.7 Electrical properties.

3.7.1 DC conductivity

DC conductivity analysis apart from electrical percolation threshold prediction could also predict the shape of the nanofiller particles incorporated into the polymer nanocomposites. From Fig. 9a one could observe that the electrical conductivity increases from the value of 10^{-11} S/cm for the neat blend ($T_{50}P_{50}$) up to 10^{-9} S/cm for the polymer nanocomposite with 3 wt% of MO particle and the increment is not

Fig. 9 **a** Variation of DC conductivity with MO loading, **b** linear $\log\sigma_{DC}$ vs $\log(p - p_c)$ plot employing the least square method, **c** $\log\sigma_{DC}$ vs $p^{-1/3}$ linear plot, **d** variation of DC conductivity for the polymer nanocomposites based upon pure PBAT ($T_0P_{100}MO_x$) and pure TPU ($T_{100}P_0MO_x$) concerning MO loading



remarkable. Increasing the MO loading up to 5 wt%, one can observe a steep jump in the value DC electrical conductivity from 10^{-9} to 10^{-5} S/cm and this steep rise could not be seen if the MO content is further increased from 5 to 10 wt% via 7 wt% instead a moderate rise could have been observed. This observation suggests that the electrical percolation threshold for the polymer nanocomposites has been reached at 5 wt% of MO content roughly.

The above phenomenon is called the “electrical double percolation phenomenon” which could be explained based on the electrical percolation theory [50, 51]. The PBAT being low melt viscous w.r.t TPU, acquires more filler resulting in the increment in the DC conductivity value, and at a certain MO loading (wt%) termed as electrical percolation threshold, there is a steep rise in the DC conductivity value at which the MO particles in the PBAT phase just touched each other to favor hovering of electrons from one particle to another resulting in a phenomenal rise in the electrical conductivity value. After crossing the percolation threshold, the steep rise in the DC conductivity value could not be noticed further instead a moderate increment in the DC conductivity is observed. In the case of pure TPU or PBAT-based nanocomposites (Fig. 9d) a certain rise could not be

observed exactly and the electrical conductivity at 10 wt% of MO loading (10^{-4} S/cm) is not as high as the case of binary polymer nanocomposite (10^{-1} S/cm). The classical power law (Eq. 3) could be recalled to find out the exact value of the electrical percolation threshold.

$$\sigma_{DC} = \sigma_0(p - p_c)^t \quad (p > p_c) \tag{4}$$

Equation 3 could be rewritten as Eq. 4 given below-

$$\log\sigma_{DC} = \log\sigma_0 + t\log(p - p_c) \tag{5}$$

linear $\log\sigma_{DC}$ vs $\log(p - p_c)$ plot employing the least square method is shown in Fig. 9b. Here p is the MO loading (wt%) in the polymer nanocomposite, p_c is the electrical percolation threshold or critical filler fraction (wt%) in the polymer nanocomposite, σ_{DC} is the DC conductivity value of the polymer nanocomposites, σ_0 is the constant termed as a scaling factor and t is critical exponent (a constant). The value of t determines the aspect ratio of the particles which are included in the polymer matrix. If value t is approximately 1.5, the nanofiller is then assumed to be spherical and if the value of t is beyond or near about 3 the aspect ratio of the nanofillers is believed to be very high which means the nanofillers are

cylindrical [21]. Now, we can find out that $t = 5.5$ is certainly greater than 3 so the MO particles are of a high aspect ratio. The electrical conductivity of polymer nanocomposites could also be analysed based on the tunneling phenomenon [52]. The nanofiller particles in a polymer nanocomposite are believed to be separated by an insulating polymer layer and with the increase in the MO content the average gap between nanofiller particles decreases and at a certain filler content known as electrical percolation threshold the interparticle gap becomes so low that free electrons on the nanofiller particle surface can easily hover to another adjacent particle facilitating the electrical conductivity mechanism. The inter-particle distance at the electrical percolation threshold is known as the tunneling distance. After upgrading the MO loading beyond the electrical percolation threshold, the interparticle distance gets further reduced but the conductivity does not increase significantly instead only the charge carrying capacity of the polymer nanocomposites gets increased. Equation 5 justifies the tunneling mechanism [53].

$$\log \sigma_{DC} \propto p^{-\left(\frac{3}{5}\right)} \quad (6)$$

Figure 9c describes the linearity in the relationship between $\log \sigma_{DC}$ and $p^{-\left(\frac{3}{5}\right)}$ justifying the tunneling mechanism according to which the logarithm of DC conductivity decreases on lowering MO loading (p).

3.7.2 AC impedance study

AC impedance measurement give the resistance felt by an LCR (Inductance Capacitance Resistance) circuit in an AC field. The study of AC impedance could also predict the electrical percolation threshold of a polymer nanocomposite when subjected to an AC field. The complex AC impedance (Z) the measurement consists of two parts: (1) real part (Z') and (2) imaginary part (Z'') and they are interrelated by Eqs. 6, 7, and 8 [54].

$$Z = iZ'' + Z' \quad (7)$$

$$Z' = Z \sin(\phi) \quad (8)$$

$$Z'' = Z \cos(\phi) \quad (9)$$

Here ϕ is the phase angle. The real part indicates the material resistivity and the imaginary part indicates the material reactance for the polymer

nanocomposites. From Eq. 6 it could be said that the AC conductivity is inversely proportional to the AC impedance and the results of the AC impedance analysis (Fig. 10a) also suggest the same where the frequency vs (Z') plots of low filler content polymer nanocomposites are more frequency-dependent starting from low-frequency value due to larger interparticle distance which is much higher than the tunneling distance causing the electron hovering mechanism directly proportional to the frequency. The polymer nanocomposite with 10 wt% of filler loading becomes almost frequency independent with the lowest (Z') value (10 Ω). Here Z' is inversely proportional to the MO loading.

Figure 10b and c describe the Z'' vs frequency plots for the polymer nanocomposites where initially Z'' is directly proportional to the frequency. At a certain frequency (Hz), Z'' attains maximum (Z''_{\max}) and again falls. The corresponding frequency for the highest Z'' is called relaxation frequency (f_r). At relaxation frequency AC to DC transition takes place and with the increase in nanofiller MO loading the value of Z''_{\max} decreases indicating there is an increment in AC conductivity. An increment in MO content leads to shifting of relaxation frequency to the right/higher frequency range. A polymer nanocomposite material is a kind of dielectric material that consists of a large number of electric-charge conducting grains with high grain boundary resistance. With the increase in the MO loading, the number of electrical-charge conducting grains increases leading to higher electrical conductivity throughout the bulk of the polymer nanocomposite but a larger number of electric-charge conducting grains takes a higher frequency to get aligned with the alternating electric field that is why the relaxation frequency of the polymer composites shifts towards the right with the increment in the filler content [55]. The radius of the Nyquist plot (Z' vs Z'' plot) describes the insulating nature of the polymer composite. The higher the radius would be the more insulating the nanocomposite would become [21]. Here Fig. 10d–h describe the Nyquist plots for the polymer nanocomposites with MO loading of 2,3,5,7 and, 10 wt% respectively. where the graphs came out to be imperfectly semi-circular due to a large number of grain boundaries and heterogeneously/co-continuously distributed electric-storage units [54, 56]. Here, we have identified the electrical percolation threshold by finding out

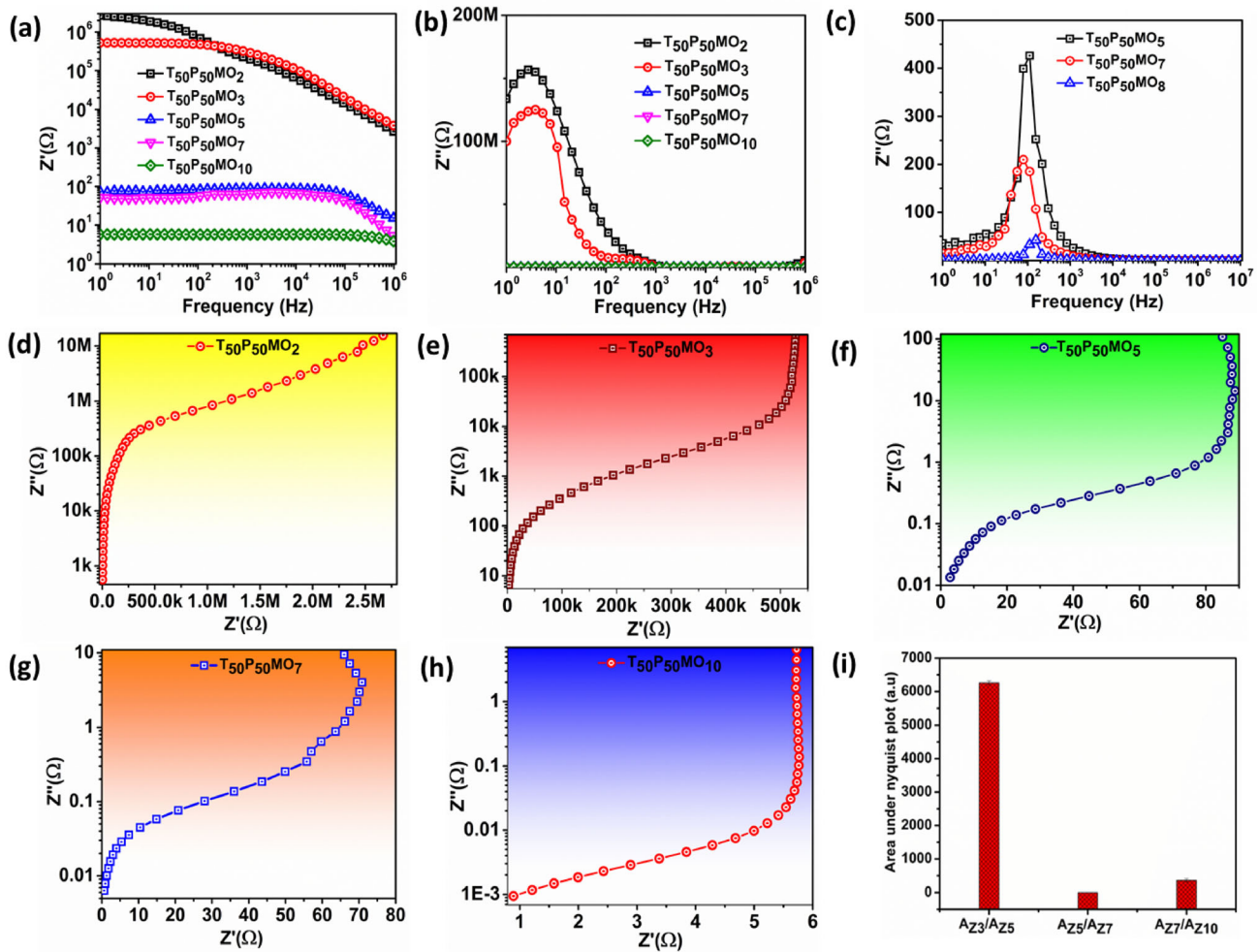


Fig. 10 a Z' vs frequency (Hz), b, c Z'' vs frequency study for polymer nanocomposites, d–h Z' vs Z'' plots of polymer nanocomposites with MO content of 3,5,7, and 10 wt%

respectively, f Study of the ratio of area under the curve of Z' vs Z'' plots of polymer nanocomposites

the area under the Z' vs Z'' curves and their ratio. The area under the curves of Z' vs Z'' plots for the polymer nanocomposites with filler loading of 2wt%, 3wt%, 5wt%, 7wt%, and 10 wt% are marked as A_{Z2} , A_{Z3} , A_{Z5} , A_{Z7} , and A_{Z10} respectively (Fig. 10i). One could observe the ratio (A_{Z3}/A_{Z5}) is about 6260 times which is the highest among A_{Z5}/A_{Z7} ($= 2.0 \pm 0.01$) times) and A_{Z7}/A_{Z10} ($= 300$ times), and a high (A_{Z3}/A_{Z5}) ratio indicates the electrical percolation threshold achieved at 5wt% of MO loading as the A_{Z5} decreases rapidly from A_{Z3} .

3.7.3 AC conductivity study

The AC conductivity (σ_{ac}) is calculated based on the data from the complex impedance analysis [54] by

Eq. 9. Where e = thickness, s = contact area of the polymer nanocomposite pellets.

$$\sigma_{ac} = \left(\frac{e}{s}\right) \left[\frac{Z'}{(Z')^2 + (Z'')^2}\right] \tag{10}$$

Figure 11 describes the AC conductivity performance of the polymer nanocomposites within the frequency range of 0 Hz to 10^7 Hz and it was found that there is a sudden increment in the conductivity value from a range of 10^{-8} – 10^{-7} Hz for polymer nanocomposite with 3 wt% of MO to a range of 10^{-4} – 10^{-3} Hz for polymer nanocomposites with 5 wt% of MO content which is believed to be the electrical percolation threshold.

The AC conductivity of the insulating blend or low MO content polymer composites is frequency-

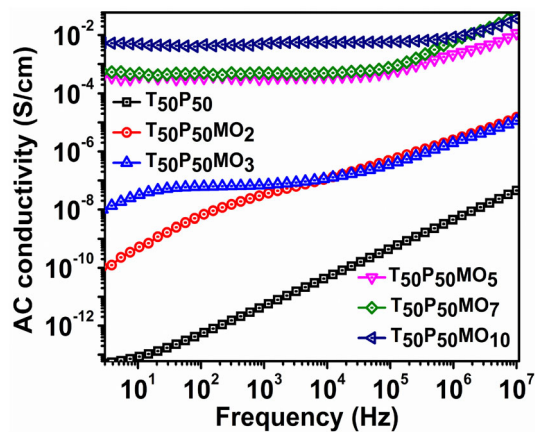


Fig. 11 Measurement of AC conductivity of the polymer nanocomposites ($T_xP_yMO_z$)

dependent at the low frequency (0–10 Hz) range because the interparticle distance is very high creating a barrier on the path of electrons hovering between adjacent particles and a little increment in the frequency results significant increment in AC conductivity as the MO particles need only up-gradation in frequency to get to close within the tunneling distance. After or near the electrical percolation threshold the interparticle distance reaches within the tunneling distance through which the electron conduction becomes easy and frequency independent at the lowest frequency range. After crossing a threshold frequency, the AC conductivity again becomes frequency independent only up to a certain extent for example Both $T_{50}P_{50}MO_5$ and $T_{50}P_{50}MO_7$ show frequency dependency around 10^5 Hz and $T_{50}P_{50}MO_{10}$ shows frequency dependency around 10^6 Hz. The highest AC conductivity around 0.04 S/cm has been shown by $T_{50}P_{50}MO_{10}$ at 10^7 Hz. To further support the AC conductivity result; dielectric constant analysis [57] and electrical modulus analysis of polymer nanocomposites were conducted and the results are shown in Fig. S2 and S3 (supporting information file).

3.8 EMI shielding studies

The medium that limits/reduce the passing of EM waves must be electrically conductive. Figure 12 gives the graphical representation of the EMI shielding performance of the polymer nanocomposites in the X-band (8.2–12.6 GHz) region of the electromagnetic radiation spectrum using a standard waveguide ($1.1 \times 2.1 \text{ cm}^2$) [50] specified for the

measurement in the X-band region in a VNA machine. The EMI shielding measurements are presented as decibels (dB) [58]. The total EMI shielding efficiency ($SE_T(\text{dB})$) is represented below as the logarithm of the ratio of transmitted power ($P(t)$) to incident power ($P(i)$) in the polymer nanocomposite shown below as Eq. 10.

$$SE_T(\text{dB}) = -10 \log \left[\frac{P(t)}{P(i)} \right] \quad (11)$$

The total EMI shielding efficiency ($SE_T(\text{dB})$) consists of absorption coefficient ($SE_A(\text{dB})$), reflection coefficient ($SE_R(\text{dB})$) and multiple reflection coefficient ($SE_M(\text{dB})$) as given in Eq. 11.

$$SE_T(\text{dB}) = SE_A(\text{dB}) + SE_R(\text{dB}) + SE_M(\text{dB}) \quad (12)$$

Here multiple reflection coefficient ($SE_M(\text{dB})$) could be neglected if the total EMI shielding efficiency ($SE_T(\text{dB})$) is less than -10 dB [50]. $SE_A(\text{dB})$ and $SE_R(\text{dB})$ could be represented as transmitted power ($P(t)$), incident power ($P(i)$) and reflected power ($P(r)$) by Eqs. 12, and 13 which could give rise to Eq. 10.

$$SE_A(\text{dB}) = 10 \log \left[\frac{P(i) - P(r)}{P(t)} \right] \quad (13)$$

$$SE_R(\text{dB}) = 10 \log \left[\frac{P(i)}{P(i) - P(t)} \right] \quad (14)$$

Shielding co-efficient terms could also be represented according to scattering (S) parameters. The reflectance (R), transmittance (T), and absorbance (A) are interrelated [55] as Eq. 14.

$$A = 1 - R - T \quad (15)$$

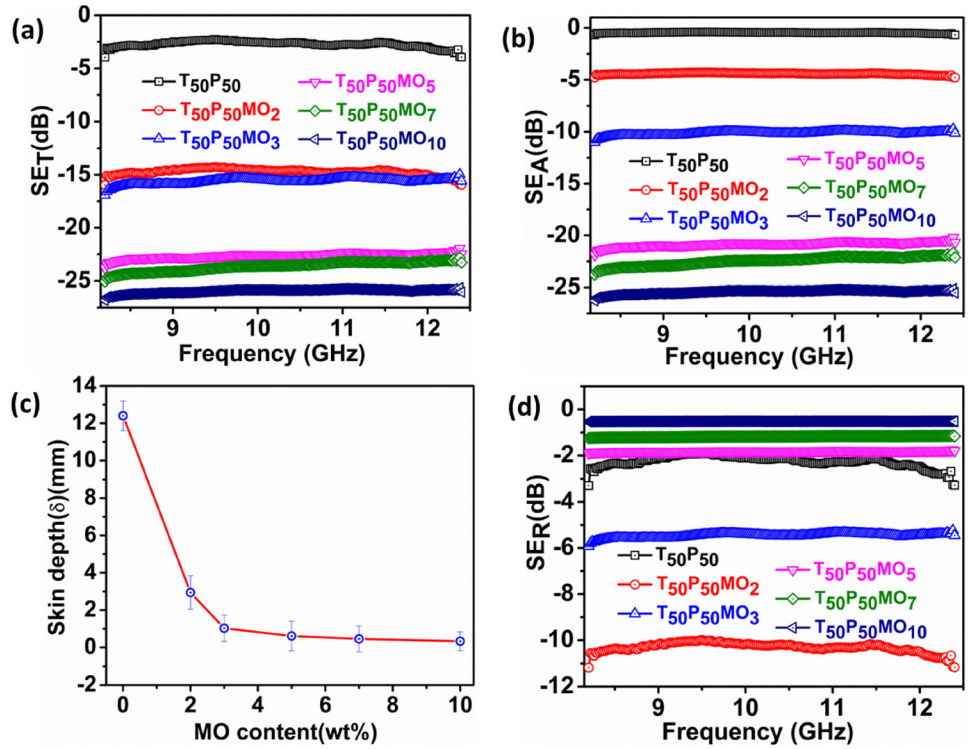
where R and T are represented in Eq. 15 and Eq. 16.

$$R = \left[\frac{P(r)}{P(i)} \right]^2 = |S_{11}|^2 = |S_{22}|^2 \quad (16)$$

$$T = \left[\frac{P(t)}{P(i)} \right]^2 = |S_{12}|^2 = |S_{21}|^2 \quad (17)$$

Here S_{11} , S_{12} , S_{22} , and S_{21} are scattering parameters known [59] as input reflection co-efficient, reverse transmission co-efficient, output reflection co-efficient, and forward transmission coefficient, respectively. Based upon scattering parameters; Eqs. 10, 11, and 12 are rewritten as Eqs. 17, 18, and 19 respectively.

Fig. 12 a SE_T , b SE_A , c SE_R performance of polymer nanocomposites in the range of X-band, d skin depth analysis of different polymer nanocomposites at 8.2 GHz of frequency



$$SE_T(dB) = 10\log \left[\frac{1}{|S_{12}|^2} \right] = 10\log \left[\frac{1}{|S_{21}|^2} \right] \tag{18}$$

$$SE_R(dB) = 10\log \left[\frac{1}{1 - |S_{11}|^2} \right] \tag{19}$$

$$SE_A(dB) = 10\log \left[\frac{1 - |S_{11}|^2}{|S_{12}|^2} \right] \tag{20}$$

The EM wave after falling upon the polymer nanocomposite surface gets penetrated and thereby loses its intensity while traveling throughout the bulk of the polymer nanocomposite. The depth at which the EM wave loses its initial intensity by (1/e) to the EM wave falling at the polymer nanocomposite surface is known as the skin depth (δ) which is mathematically represented below as Eq. 20.

$$\delta = \left[\frac{1}{\sqrt{(\pi \cdot f \cdot \mu \cdot \sigma)}} \right] \tag{21}$$

Here f , μ , and σ signify frequency, EM wave permittivity, and electrical conductivity respectively. The δ could also be related to the absorption coefficient of the EM wave according to Eq. 21.

$$SE_A = -8.68 \left[\frac{t}{\delta} \right] \tag{22}$$

Here t = thickness of the polymer nanocomposite sample given in millimeters.

The electrical conductivity of polymer nanocomposites plays a pivotal role to decide their EMI shielding performance as shown in Fig. 12a, the polymer nanocomposite with 3 wt% of MO content showed EMI shielding efficiency in the range of -17 ± 0.01 dB whereas the polymer blend has the shielding efficiency of -3.0 ± 0.01 dB. A sudden jump in the value of EMI shielding value (SE_T) to -24 dB from -17 ± 0.01 dB could be seen as the MO loading is increased to 5 wt% from 3wt% indicating the electrical percolation threshold has been reached after which the EMI shielding value did not increase significantly. The highest SE_T is shown by the polymer nanocomposite with filler loading of 10 wt% for which the value of SE_T being -30 dB at 8.2 GHz of frequency. Figure 12b and d give the information about the change of SE_A and SE_R with the change in the frequency for the polymer nanocomposites in the X-band region and it was found that the absorption mechanism dominates the SE_T values with an increase in MO loading. Figure 12c gives information regarding the skin depth of polymer nanocomposites

with an increase in MO content whereas the skin depth decreases with an increase in MO loading. The more the polymer nanocomposite is electrically conductive the less would be its skin depth and EMI shielding efficiency. From the skin depth values, one can observe there is no significant decrease in skin depth after the MO loading surpasses 5 wt% and the skin depth remains around 0.3 mm signifying the 5 wt% loadings is the electrical percolation threshold.

Figure 13a graphically represents the EMI shielding mechanism of polymer nanocomposites where reflected, absorbed and transmitted waves are graphically portrayed and MO are preferentially distributed into the PBAT phase into the co-continuous morphology creating an easy electrically conductive network. At the frequency of 8.2 GHz (Fig. 13b), the total shielding efficiency is dominated by SE_A with 98% of absorbance for the polymer nanocomposite with 10 wt% of MO loading whereas at low MO content the total EMI shielding efficiency is dominated primarily by reflection co-efficient.

3.8.1 Nicholson-Ross-Weir (NRW) conversion method

NRW method is used to calculate complex permittivity ($E(r)$) and complex permeability ($\mu(r)$) from the scattering parameters which we get from VNA during EMI shielding analysis. We need to calculate $E(r)$ and $\mu(r)$ in a stepwise manner [60]. We can write down the relationship between scattering parameters, reflection coefficient, and transmission coefficient in Eqs. 22 and 23.

$$S_{11} = \left\{ \frac{\Gamma(1 - T^2)}{(1 - \Gamma^2 T^2)} \right\} \quad (23)$$

$$S_{21} = \left\{ \frac{T(1 - \Gamma^2)}{(1 - \Gamma^2 T^2)} \right\} \quad (24)$$

The reflection coefficient (Γ) could be evaluated from Eq. 24 from here the value of root $X = |\Gamma_1| < 1$ is the criteria.

$$\Gamma = X \pm \sqrt{(X^2 - 1)} \quad (25)$$

The exact value of the root X is related to scattering parameters and given as Eq. 25.

$$X = \left[\frac{(S_{11}^2 - S_{21}^2) + 1}{2S_{11}} \right] \quad (26)$$

The transmission coefficient (T) could also be written as Eq. 26.

$$T = \left[\frac{(S_{11} + S_{21}) - \Gamma}{1 - (S_{11} + S_{21})\Gamma} \right] \quad (27)$$

If Υ is the complex propagation constant which is represented below as Eqs. 27 and 28.

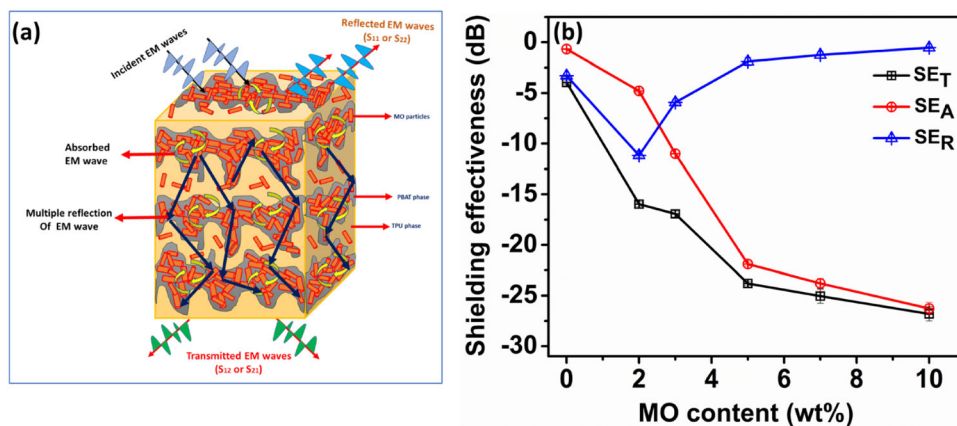
$$\frac{1}{\Lambda} = \left(\frac{\Upsilon}{i2\pi} \right) = i \left[\left(\frac{1}{2\pi L} \right) \ln \left(\frac{1}{T} \right) \right] \quad (28)$$

$$\frac{1}{\Lambda^2} = - \left\{ \left(\frac{1}{2\pi L} \right) \ln \left(\frac{1}{T} \right) \right\}^2 \quad (29)$$

Here L ($= 0.8$ mm) is the thickness of the polymer nanocomposite sheet. Complex permittivity and complex permeability are interrelated as given in Eq. 29.

$$\frac{1}{\Lambda^2} = \left[\frac{E(r) \cdot \mu(r)}{\lambda_0^2} - \frac{1}{\lambda_c^2} \right] \quad (30)$$

Fig. 13 a Graphical representation of EMI shielding mechanism of polymer nanocomposites, b comparative study of the contribution of different EMI shielding co-efficient with MO loading for the polymer nanocomposites



Here λ_c is the cut-off frequency for the waveguide of the X-band and it is equal to 6.557 GHz and λ_0 is the free-space wavelength. From Eq. 30 we get Eq. 31 representing complex permeability which is further modified to Eq. 32 to calculate the complex permittivity.

$$\frac{1}{\Lambda^2} = \mu(r)^2 \left[\frac{(1 - \Gamma_1)^2}{(1 + \Gamma_1)^2} \right] \left[\frac{1}{\lambda_0^2} - \frac{1}{\lambda_c^2} \right] \tag{31}$$

$$\mu(r) = \frac{1}{\Lambda} \left[\left\{ \frac{(1 + \Gamma_1)}{(1 - \Gamma_1)} \right\} \right] \sqrt{\left[\frac{1}{\left(\frac{1}{\lambda_0^2} - \frac{1}{\lambda_c^2} \right)} \right]} \tag{32}$$

Then from Eqs. 30 and 31, we get Eq. 32 which gives the complex permittivity.

$$E(r) = \mu(r) \left[\frac{(1 - \Gamma_1)^2}{(1 + \Gamma_1)^2} \right] \left(1 - \frac{\lambda_0^2}{\lambda_c^2} \right) \left(\frac{\lambda_0^2}{\lambda_c^2} \mu(r) \right) \tag{33}$$

The values of complex permittivity and permeability for the polymer nanocomposites with frequency (X-band) are represented below in Fig. 14 where the frequency vs E' shows (Fig. 14a) a negligible increment in the real part of permittivity with MO loading but interestingly the loss component of permittivity (E'') increases noticeably with MO

loading and abruptly attains a high value after 5 wt% of filler loading signifying it as the electrical percolation threshold at which the loss factor dominates due to sudden increment in electrical conductivity portrays a sudden involvement of a large number of electrically polarizable mobile charge carriers contributing to the conductance loss mainly in the PBAT phase of the polymer nanocomposite [61].

A similar trend is also observed in the case of the permeability study (Fig. 14c and d) where the loss component μ'' initially remained low if the MO content is kept low and suddenly jumps to a higher value after crossing the MO loading of 5 wt%. This observation is directly attributed to the increment in electrical conductivity of the polymer nanocomposites with filler loading [62]. With the increment in the frequency both the storage and loss component of permeability decreases because at the high-frequency range the electrode polarization of mobile charge carriers could not contribute to the permeability [55]. The tangent loss of complex permeability (Fig. 14e) also indicates the electrical percolation threshold at 5 wt% filler loading when the tangent value certainly jumps to a higher value in the range of 2.0 ± 0.001 to 2.9 ± 0.002 from a range of 1.2 ± 0.0012 to 1.5 ± 0.001 . The tangent loss is expressed as Eq. 33.

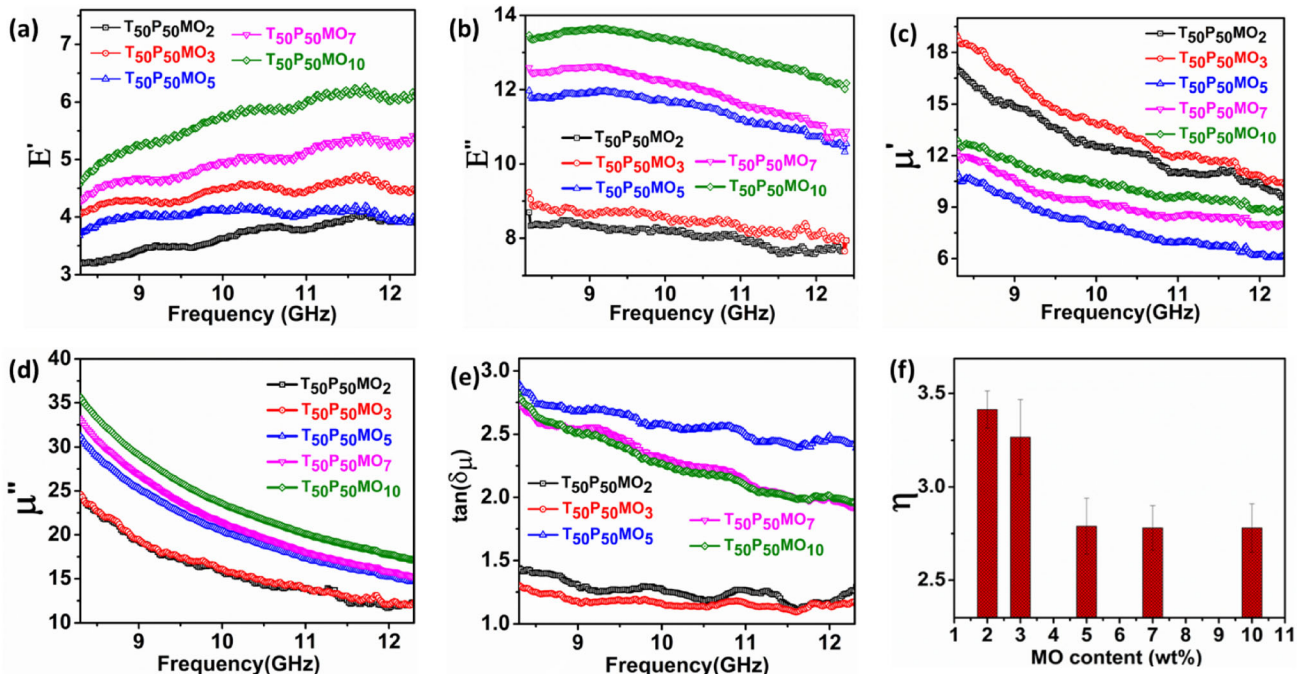


Fig. 14 a E' vs frequency, b E'' vs frequency c μ' vs frequency, d μ'' vs frequency, e $\tan(\delta_\mu)$ vs frequency plot of the polymer nanocomposites in the X-band region of the electromagnetic spectrum, f impedance matching co-efficient at different filler loading

$$\tan(\delta_\mu) = \left(\frac{\mu''}{\mu'} \right) \quad (34)$$

Another important analysis of the electrical percolation threshold is impedance matching co-efficient (η) which is defined in Eq. 34.

$$\eta = \left[\left| \frac{Z}{Z_0} \right| \right] \quad (35)$$

Here Z is the impedance of polymer nanocomposite shielding material and Z_0 is the impedance of the vacuum. Both Z and Z_0 are mathematically presented as Eqs. 35 and 36.

$$Z_0 = \sqrt{\left(\frac{\mu_0}{\epsilon_0} \right)} \quad (36)$$

$$Z = \sqrt{\left(\frac{\mu(r) \cdot \mu_0}{\epsilon(r) \cdot \epsilon_0} \right)} \quad (37)$$

The decreasing η values signify the improvement in the electrical properties of the polymer nanocomposites. From the Fig. 14f it is clear that the increment in the MO loading improves the electrical property of the polymer nanocomposite as the η value decreases to 2.8 ± 0.01 from 3.27 ± 0.003 if the MO loading is increased from 3 to 5 wt% of MO loading after which the value of η becomes constant and almost unchanged at 2.78 indicating 5 wt% being the electrical percolation threshold.

4 Potential applications of biodegradable polymer nanocomposite materials

These type of biodegradable polymer nanocomposites have potential applications in medical sectors as a EMI shield materials to protect different electronic equipment in teaching hospitals [63]. In our previous work we have produced a 433 MHz transmitter-receiver module which has a potential application as a EMI shield material under the EM frequency range of 433 MHz [64].

5 Conclusion

A copious study on the mechanical properties, electrical properties, EMI shielding properties and biodegradability of binary polymer nanocomposites

based on PBAT and TPU with the variation in the amount of oxidized MWCNT (MO) has been portrayed in this research article. The MO particles were found to be preferentially distributed into the PBAT phase.

- The preferential distribution of MO particles in the PBAT phase was supported by FTIR, DMA, FESEM, HRTEM, and selective dissolution tests.
- The FTIR study showed the disappearance of the peak corresponding to PBAT ester carbonyl stretching frequency at 1710 cm^{-1} in the polymer nanocomposites signifying the preferential distribution of MO particles in the PBAT phase.
- DMA study proved the preferential distribution of MO particles in the PBAT phase as the tangent loss peak around $-20 \text{ }^\circ\text{C}$ corresponding to PBAT being gradually depleted more compared to that of TPU with the addition of MO particles.
- The FESEM and HRTEM images showed darker cloud-like portions of the PBAT phase being enriched with MO particles which are evidenced by the selective dissolution test.
- A proper justification of the formation of the “electrical double percolation” phenomenon comes with the very low electrical percolation threshold of the polymer nanocomposites at just 5 wt% of MO loading indicated by a certain jump in the electrical conductivity from 10^{-9} to 10^{-5} S/cm on increasing the MO content from 3 to 5 wt% in the polymer nanocomposites.
- AC conductivity analysis, AC impedance analysis, dielectric constant analysis, and electrical modulus analysis indicated the electrical percolation threshold being at 5wt% of MO loading.
- The electrical percolation threshold of the polymer nanocomposites was also marked by a certain jump in the value of SE_T from -17 dB to -24 dB on increasing the MO loading from 3 to 5 wt%.
- With 10 wt% of MO loading -30 dB of SE_T is achieved by a mere 0.8 mm thick polymer nanocomposite film.
- NRW analysis showed permittivity and permeability study of the polymer nanocomposites to further indicate the electrical percolation threshold.

The enzyme-mediated biodegradability study showed an increment in biodegradation with MO loading.

Acknowledgements

Narayan Ch. Das also thanks the SERB-DST (Grand No. ECR/2016/000048), Govt. of India for the financial support. KN acknowledges the Indian Institute of Technology- Kharagpur (IIT-KGP) for providing financial support. All authors want to thank Central Research Facility (CRF) for all of the technical facilities.

Author contributions

KN has innovated the research topic, conducted the processing methods, written the manuscript, conducted EMI shielding, conductivity measurements. SKG conducted SEM, TEM measurements, AK conducted FTIR, DMA measurements. PD conducted rest of the experiment. NCD supervised the whole work. All the authors read and approved the final manuscript.

Funding

Funding was provided by SERB-DST (Grand No. CRG/2021/003146), Govt. of India.

Data availability

Data will be available if any request is made.

Declarations

Conflict of interest We hereby confirm that there are no conflicting financial interests or personal relationships that would have rebutted the work reported in this research article.

Ethical approval This research article does not promote any experiment done on animals or human participants.

Supplementary Information: The online version contains supplementary material available at <http://doi.org/10.1007/s10854-023-10212-4>.

References

1. K. Nath, S. Ghosh, S.K. Ghosh, P. Das, N.C. Das, *J. Appl. Polym. Sci.* **138**, 50514 (2021)
2. T. Saunders, *Complement. Ther. Nurs. Midwifery* **9**, 191–197 (2003)
3. S.C. Jana, A. Pietro, *J. Appl. Polym. Sci.* **86**, 2159–2167 (2002)
4. S.H. Park, P.R. Bandaru, *Polymer* **51**, 5071–5077 (2010)
5. W. Zhou, Y. Wu, F. Wei, G. Luo, W. Qian, *Polymer* **46**, 12689–12695 (2005)
6. R.K. Layek, A.K. Nandi, *Polymer* **54**, 5087–5103 (2013)
7. A. Li, Z. Feng, Y. Sun, L. Shang, L. Xu, *J. Power Sources* **343**, 424–430 (2017)
8. G.A. Jimenez, S.C. Jana, *Polym Eng Sci.* **49**, 2020–2030 (2009)
9. S. Iijima, *Nature* **354**, 56–58 (1991)
10. S. Iijima, T. Ichihashi, *Nature* **363**, 56–58 (1993)
11. P. Pisitsak, R. Magaraphan, S.C. Jana, *J. Nanomater.* **2**, 2 (2012)
12. C. Penu, G.-H. Hu, A. Fernandez, P. Marchal, L. Cholin, *Polym Eng Sci.* **52**, 2173–2181 (2012)
13. N.C. Das, Y. Liu, K. Yang, W. Peng, S. Maiti, H. Wang, *Polym Eng Sci.* **49**, 1627–1634 (2009)
14. A.S. Zeraati, A.M. Anjaneyalu, S.P. Pawar, A. Abouelmagd, U. Sundararaj, *Polym Eng Sci.* **61**, 959–970 (2021)
15. A.K. Mohanty, A. Ghosh, P. Sawai, K. Pareek, S. Banerjee, A. Das, P. Pötschke, G. Heinrich, B. Voit, *Polym Eng Sci.* **54**, 2560–2570 (2014)
16. S.S. Chauhan, M. Verma, P. Verma, V.P. Singh, V. Choudhary, *Polym Adv Technol.* **29**, 347–354 (2018)
17. H. Mei, M. Lu, S. Zhou, L. Cheng, *J. Appl. Polym. Sci.* **138**, 50033 (2021)
18. T. Jeevananda, N.H. Kim, S.-B. Heo, J.H. Lee, *Polym Adv Technol.* **19**, 1754–1762 (2008)
19. L. Monnereau, L. Urbanczyk, J.M. Thomassin, T. Pardoën, C. Bailly, I. Huynen, C. Jérôme, C. Detrembleur, *Polymer* **59**, 117–123 (2015)
20. J. Jang, J.E. Cha, S.H. Lee, J. Kim, B. Yang, S.Y. Kim, S.H. Kim, *Polymer* **186**, 122030 (2020)
21. R. Ravindren, S. Mondal, K. Nath, N.C. Das, *Compos. A: Appl. Sci. Manuf.* **118**, 75–89 (2019)
22. F. Xiang, Y. Shi, X. Lia, T. Huang, C. Chen, Y. Peng, Y. Wang, *Eur. Polym. J.* **48**, 350–361 (2012)
23. K. Zhang, G.H. Li, L.M. Feng, N. Wang, J. Guo, K. Sun, K.X. Yu, J.B. Zeng, T. Li, Z. Guo, M. Wang, *J. Mater. Chem. C* **5**, 9359–9369 (2017)

24. C. Roman, M.G. Morales, M.A. Olariu, T. McNally, *J. Mater. Sci.* **55**, 2966–2976 (2020)
25. M.A.B.S. Nunes, B.R. de Matos, G.G. Silva, E.N. Ito, T.J.A. de Melo, G.J.M. Fachine, *Polym. Compos* **42**, 661–677 (2021)
26. A.M. Kunjappan, A. Reghunadhan, A.A. Ramachandran, L. Mathew, M. Padmanabhan, D. Laroze, S. Thomas, *Polym Adv Technol.* **33**, 976–979 (2022)
27. R. Dou, Y. Shao, S. Li, B. Yin, M. Yang, *Polymer* **83**, 34–39 (2016)
28. A. Kumar, V. Choudhary, R. Khanna, S.N. Tripathi, M. Ikram-Ul-Haq, V. Sahajwalla, *J. Appl. Polym. Sci.* **133**, 43389 (2016)
29. C. Ma, W. Zhang, Y. Zhu, Li. Ji, R. Zhang, N. Koratkar, J. Liang, *Carbon N Y* **46**, 406–410 (2008)
30. R. Ravindren, S. Mondal, P. Bhawal, S.M.N. Ali, N.C. Das, *Polym. Compos.* **40**, 1404–1418 (2019)
31. X.L. Xie, Y.W. Mai, X.P. Zhou, *Mater. Sci. Eng. R Rep.* **49**, 89–112 (2005)
32. A. Pistone, A. Ferlazzo, M. Lanza, C. Milone, D. Iannazzo, A. Piperno, E. Piperopoulos, S. Galvagno, *J. Nanosci. Nanotechnol.* **12**, 5054–5060 (2012)
33. R. Ravindren, S. Mondal, K. Nath, N.C. Das, *Compos. Part A Appl. Sci.* **118**, 75–89 (2019)
34. P. Scherrer, *Nachr. Ges. Wiss. Göttingen.* **26**, 98–100 (1918)
35. J.I. Langford, A.J.C. Wilson, *J. Appl. Cryst.* **11**, 102–113 (1978)
36. B.D. Cullity, *Elements of X-Ray Diffraction*, 2nd edn. (Addison Wesley, Reading, MA, USA, 1956), p.284
37. N.T. Kilic, B.N. Can, M. Kodal, G. Ozkoc, *J. Appl. Polym. Sci.* **136**, 47217 (2019)
38. Y.D. Shi, M. Lei, Y.F. Chen, K. Zhang, J.B. Zeng, M. Wang, *Phys. Chem. C.* **121**, 3087–3098 (2017)
39. V. Jašo, M. Cvetinovic, S. Rakić, Z.S. Petrović, *J. Appl. Polym. Sci.* **131**, 1–8 (2014)
40. C.Y. Khor, Z.M. Ariff, F.C. Ani, M.A. Mujeebu, M.K. Abdullah, M.Z. Abdullah, M.A. Joseph, *Int. Commun. Heat Mass Transf.* **37**, 131–139 (2010)
41. O. Gershevit, C.N. Sukenik, *J Am Chem Soc.* **126**, 482–483 (2004)
42. R.R. Krishni, K.Y. Foo, B.H. Hameed, *Desalin. Water Treat.* **52**, 6104–6112 (2014)
43. A. Tomova, G. Gentile, A. Grozdanov, M.E. Errico, P. Paunovic, M. Avella, A.T. Dimitrov, *Acta Phys. Pol.* **129**, 405 (2016)
44. S.K. Abdel-Aal, A.S. Abdel-Rahman, *J Nanopart Res.* **22**, 267 (2020)
45. S.K. Abdel-Aal, M.F. Kandeel, A.F. El-Sherif, A.S. Abdel-Rahman, *Phys. Status Solidi* **218**, 210038 (2021)
46. L.B. Tavares, N.M. Ito, M.C. Salvadori, D.J. dos Santos, D.S. Rosa, *Polym. Test.* **67**, 169–176 (2018)
47. A. Haryńska, J. Kucinska-Lipka, A. Sulowska, I. Gubanska, M. Kostrzewa, H. Janik, *Mater.* **12**, 887 (2019)
48. G. Zehetmeyer, S.M.M. Meira, J.M. Scheibel, R.V. Bof de Oliveira, A. Brandelli, R.M.D. Soares, *J. Appl. Polym. Sci.* **133**, 43212 (2016)
49. A.S. Abdel-Rahman, *Int. J. Comput. Methods Eng.* **24**, 155–166 (2023)
50. Y. Liu, H. He, G. Tian, Y. Wang, J. Gao, C. Wang, L. Xu, H. Zhang, *Compos Sci Technol.* **214**, 108956 (2021)
51. D.I. Moubarak, H.H. Hassan, T.Y. El-Rasasi, H.S. Ayoub, A.S. Abdel-Rahaman, S.A. Khairy, Y.H. Elbasha, *Nonlinear Optics, Nonlinear Opt. Quantum Opt.* **53**, 31–59 (2021)
52. N. Ryvkina, I. Tchmutin, J. Vilčáková, M. Pelíšková, P. Sába, *Synth. Met.* **148**, 141–146 (2005)
53. S. Ganguly, S. Ghosh, P. Das, T.K. Das, S.K. Ghosh, N.C. Das, *Polym. Bull.* **77**, 2923–2943 (2020)
54. S. Nasri, A.L.B. Hafsia, M. Tabellout, M. Megdiche, *RSC Adv.* **6**, 76659–76665 (2016)
55. C.K. Madhusudhan, K. Mahendra, N. Raghavendra, M. Revanasiddappa, M. Faisal, *J. Mater. Sci.: Mater. Electron.* **33**, 1366–1382 (2022)
56. Z. Bo, Z. Wen, H. Kim, G. Lu, K. Yu, J. Chen, *Carbon N Y.* **50**, 111–116 (2021)
57. S.K. Abdel-Aal, A.S. Abdel-Rahman, *J. Mater. Sci.: Mater. Electron.* **48**, 1686–1693 (2019)
58. B.V. Bhaskara Rao, M. Chengappa, S.N. Kale, *Mater. Res. Express.* **4**, 045012 (2017)
59. S. Koul, R. Chandra, S.K. Dhawan, *Polymer* **41**, 9305–9310 (2000)
60. A. Singh, S. Bose, M. Gupta, R.S. Gupta, *Microw. Opt. Technol. Lett.* **33**, 54–57 (2002)
61. A.C. Fadhil, R.J. Akram, A.A. Sabreen, *Energy Procedia* **119**, 52 (2017)
62. J. Huo, L. Wang, H. Yu, *J. Mater. Sci.* **44**, 3917–3927 (2009)
63. C.K. Azah, J.K. Amoako, F. Sam, *Radiat Prot Dosim.* **183**, 348–354 (2019)
64. K. Nath, S.K. Ghosh, A. Katheria, P. Das, S.N. Chowdhury, P. Hazra, S. Azam, N.C. Das, *Polym. Adv. Technol.* **34**, 1019–1034 (2023)

Publisher's Note Springer Nature remains neutral with regard to jurisdictional claims in published maps and institutional affiliations.

Springer Nature or its licensor (e.g. a society or other partner) holds exclusive rights to this article under a publishing agreement with the author(s) or other rightsholder(s); author self-archiving of the accepted manuscript version of this article is solely governed by the terms of such publishing agreement and applicable law.